The Journal of Chemical Physics

Role of exchange and correlation in high-harmonic generation spectra of H_2, N_2, and CO_2: Real-time time-dependent electronic-structure approaches

Cite as: J. Chem. Phys. **154**, 014101 (2021); https://doi.org/10.1063/5.0033072
Submitted: 13 October 2020 . Accepted: 11 December 2020 . Published Online: 04 January 2021

Carlo Federico Pauletti, Emanuele Coccia, and Eleonora Luppi

The Journal of Chemical Physics ARTICLE scitation.org/journal/jcp

Role of exchange and correlation in high-harmonic generation spectra of H_2, N_2, and CO_2: Real-time time-dependent electronic-structure approaches

Cite as: J. Chem. Phys. 154, 014101 (2021); doi: 10.1063/5.0033072
Submitted: 13 October 2020 • Accepted: 11 December 2020 •
Published Online: 4 January 2021

Carlo Federico Pauletti,[1,2] Emanuele Coccia,[1] and Eleonora Luppi[2,a)]

AFFILIATIONS

[1] Dipartimento di Scienze Chimiche e Farmaceutiche, Via Giorgieri 1, Trieste Italy
[2] Laboratoire de Chimie Théorique, Sorbonne Université and CNRS, F-75005 Paris, France

[a)] **Author to whom correspondence should be addressed:** eleonora.luppi@upmc.fr

ABSTRACT

This study arises from the attempt to answer the following question: how different descriptions of electronic exchange and correlation affect the high-harmonic generation (HHG) spectroscopy of H_2, N_2, and CO_2 molecules? We compare HHG spectra for H_2, N_2, and CO_2 with different *ab initio* electronic structure methods: real-time time-dependent configuration interaction and real-time time-dependent density functional theory (RT-TDDFT) using truncated basis sets composed of correlated wave functions expanded on Gaussian basis sets. In the framework of RT-TDDFT, we employ Perdew-Burke-Ernzerhof (PBE) and long-range corrected Perdew-Burke-Ernzerhof (LC-ωPBE) functionals. We study HHG spectroscopy by disentangling the effect of electronic exchange and correlation. We first analyze the electronic exchange alone, and in the case of RT-TDDFT with LC-ωPBE, we use $\omega = 0.3$ and $\omega = 0.4$ to tune the percentage of long-range Hartree–Fock exchange and short-range exchange PBE. Then, we added the correlation as described by the PBE functional. All the methods give very similar HHG spectra, and they seem not to be particularly sensitive to the different description of exchange and correlation or to the correct asymptotic behavior of the Coulomb potential. Despite this general trend, some differences are found in the region connecting the cutoff and the background. Here, the harmonics can be resolved with different accuracy depending on the theoretical schemes used. We believe that the investigation of the molecular continuum and its coupling with strong fields merits further theoretical investigations in the near future.

I. INTRODUCTION

The optical response of a molecular system in intense ultrashort laser fields is a subject of increasing interest since the advent of attosecond (10^{-18} s) laser pulse generation, characterization, and application.[1–4] In fact, the recent impressive advances in laser technology are continuously triggering the introduction of new time-resolved spectroscopies, which offer the opportunity to investigate electron dynamics with unprecedented time resolution.[5–11]

Attosecond pulses may be obtained via the nonlinear optical process high-harmonic generation (HHG), which can be understood semi-classically as a sequence of three steps (three-step model, 3SM): (1) electron ionization in a strong infrared (IR) field, (2) electron acceleration due to the laser field, and (3) electron recombination with the parent ion. During the recombination, coherent extreme ultraviolet (XUV) and soft x-ray radiations with a sub-femtosecond temporal resolution, i.e., HHG, are emitted.[12,13]

The electron dynamics implicated in the HHG process can be rather complex.[10,14–17] Indeed, when the laser interacts with

the system, a non-stationary electronic wavepacket, consisting of a coherent superposition of excited states, is generated. The time-evolution of the wavepacket involves changing interference and coupling between the different excited states. Moreover, the wavepacket dynamics is determined by parameters of the laser such as intensity, duration, polarization, and phase of carrier frequency.

The proper treatment of the time-dependent electronic wavepacket, and therefore of the many-electron dynamics, under the influence of the laser field is obtained by propagating the time-dependent Schrödinger equation (TDSE). Real-time time-dependent electronic-structure approaches can be conceptually separated in two classes: (1) real-time time-dependent wave function (RT-TDWF) based methods[18–35] and (2) real-time time-dependent density functional theory (RT-TDDFT).[36–46] In RT-TDWF, the many-electron dynamics is described by a correlated time-dependent wave function, while in RT-TDDFT, the key quantity is the time-dependent density.

Another essential theoretical/computational aspect, common to RT-TDWF and RT-TDDFT, is the strategy used to solve the TDSE. In fact, time propagation can be directly applied to the molecular orbitals (and the amplitudes)[26,31–33] or to a truncated basis composed of the ground- and excited-state correlated wave functions of the field-free electronic Hamiltonian.[18,19,21,47–49] In the last mentioned approach, for RT-TDDFT, the excited states are derived in the linear-response Kohn–Sham (KS) framework.[50] In practice, the wave functions are never explicit, but only the TDDFT excitation energies and transition dipole moments are used in the propagation.[18]

In the framework of RT-TDWF, most of the theoretical approaches developed are given by the time-dependent extension of the well-established methods: configuration interaction (CI), coupled cluster (CC), and multiconfigurational self-consistent field (MCSCF).[26,27,31,35,51–53] Recently, RT-TDWF methods have been applied to investigate HHG in atoms and molecules. The importance of electron correlation in HHG for He, Be, and Ne atoms was investigated by Sato *et al.*[27] using the real-time time-dependent complete-active-space self-consistent-field (RT-TD-CASSCF) method and for Ne and Ar atoms by Pathak *et al.*[53] with the time-dependent coupled-electron pair approximation with optimized orbitals (TD-OCEPA0) method. Luppi and Head-Gordon[18] also investigated the role of electron correlation in H_2 and N_2 by using real-time time-dependent configuration interaction with single (RT-TD-CIS) and perturbative-double [RT-TD-CIS(D)] excitations and real-time time-dependent equation-of-motion coupled-cluster singles and doubles (RT-TD-EOM-CCSD) methods. RT-TD-CIS has been used by some of us to describe the Cooper minimum in the HHG spectrum of an Ar atom at different laser intensities.[54] The role of electron correlation in HHG of CO_2 has been investigated by means of the real-time time-dependent propagation of algebraic-diagrammatic construction (ADC) states.[24] The role of HHG as a probe for isomers of polyatomic organic molecules was investigated by Bedurke *et al.*[29] using RT-TD-CIS and by Wong *et al.*[28] using a multielectron wave function coupled to the Cartesian grid approach.

In the framework of RT-TDDFT, the real interacting many-electron system is usually described by a non-interacting KS system able to reproduce the same density. In the case of a direct propagation, the TDDFT solution of the TDSE for the real system is replaced by the solution of a time-dependent equation, which propagates the time-dependent KS orbitals.[55,56] The many-electron effects are encoded in the time-dependent exchange–correlation potential v_{xc}, which is a functional of the density, and also, in principle, depends on all previous times. However, in most of the cases, the adiabatic approximation is used, i.e., v_{xc} is evaluated at the instantaneous time-dependent density.[57]

To accurately describe the strong-field electron dynamics in RT-TDDFT, it is necessary to correctly reproduce the long-range behavior of v_{xc}. This permits to reproduce the ionization threshold energy, giving the onset of the continuum spectrum. Different strategies have been introduced such as self-interaction corrections (SIC),[58,59] range-separated functionals,[60–63] and long-range corrected potentials.[64,65]

Instead, the RT-TDDFT approaches that propagate a truncated eigenstate basis, constructed from linear-response TDDFT, describe the many-electron effects through the exchange–correlation kernel f_{xc}. f_{xc} is the functional derivative of v_{xc} with respect to the density and also needs to be approximated. f_{xc} is nonlocal in time and space, but the most common approximations are adiabatic, and only the nonlocality in space is taken into account. In particular, range-separated approaches are among the most successful schemes to model the space dependence. Usually, in these approaches, the exchange part of f_{xc}, i.e., f_x, is decomposed in a long-range (lr) Hartree–Fock (HF) and a short-range (sr) DFT component: $f_x = f_{x,HF}^{lr} + f_x^{sr}$. The long-range nonlocal exchange kernel permits to better describe Rydberg and ionization potentials, but the lack of frequency-dependence prevents the treatment of doubly excited states.[57]

Recently, RT-TDDFT has been applied to investigate HHG molecules. Monfared *et al.*[66] studied the effects of inner orbitals in the HHG spectra for N_2O and, in particular, the role of valence electrons as a way to extend the harmonic plateau by using TDDFT with SIC correction to v_{xc} in the local-density approximation (LDA). The role of inner-valence molecular orbitals was also studied by Chu and Groenenboom[67] for the HHG spectra of N_2. In this case, the LB_α exchange–correlation potential was used for a correct representation of the continuum states. Gorman *et al.*[68] investigated the structural properties of CO_2, N_2O, and OCS molecules in combination with HHG spectroscopy using TDDFT with SIC corrections to the LDA v_{xc}. Luppi and Head-Gordon[18] also investigated the role of electron correlation in H_2 and N_2 by using RT-TDDFT.

In this work, we have investigated the role of exchange and correlation in the HHG spectra of H_2, N_2, and CO_2 molecules (at fixed internuclear separation) with RT-TD-CIS and RT-TDDFT using a truncated basis composed of the ground- and excited-state correlated wave functions of the field-free electronic Hamiltonian. This basis is represented using Gaussian functions adapted for strong-field processes.[69] At the RT-TDDFT level, we have studied the effect of the exchange and correlation on the HHG spectra by means of the Perdew-Burke-Ernzerhof (PBE)[59] and long-range corrected long-range corrected Perdew-Burke-Ernzerhof (LC-ωPBE) functionals, i.e., by means of RT-TD-PBE and RT-TD-LC-ωPBE.[60,61] The LC-ωPBE is a range-separated functional, which permits to tune the long-range exchange HF and the short-range exchange–correlation DFT functionals.

This article is organized as follows: in Sec. II, we introduce the formalism of RT-TD-CIS and RT-TDDFT. The computational method is described in Sec. III, and the results are discussed in Sec. IV. Finally, in Sec. V, conclusions and perspectives are given. Unless otherwise indicated, atomic units are used throughout this paper.

II. THEORY

The time-dependent Schrödinger equation for a molecular system perturbed by an external time-dependent electric field is given by

$$i\frac{\partial|\Psi(t)\rangle}{\partial t} = \left(\hat{H}_0 + \hat{V}(t)\right)|\Psi(t)\rangle, \tag{1}$$

where $\hat{H}_0$ is the time-independent field-free Hamiltonian and $\hat{V}(t) = -\hat{\boldsymbol{\mu}}\cdot\mathbf{E}(t)$ is the time-dependent potential in the length gauge, written in terms of the molecular dipole and the time-dependent electric field $\mathbf{E}(t)$.[18]

We have considered a linearly polarized electric field $\mathbf{E}(t)$ along the α axis (α = x, y or z), representing a laser pulse,

$$\mathbf{E}(t) = E_0\mathbf{n}_\alpha \sin(\omega_0 t + \phi) f(t), \tag{2}$$

where E_0 is the maximum field strength, $\mathbf{n}_\alpha$ is a unit vector along the α axis, ω_0 is the carrier frequency, ϕ is the phase, and $f(t)$ is the envelope function chosen as

$$f(t) = \begin{cases} \cos^2\left(\frac{\pi}{2\sigma}(\sigma - t)\right) & \text{if } |t-\sigma| \le \sigma \\ 0 & \text{else,} \end{cases} \tag{3}$$

where σ is the width of the field envelope.

To solve Eq. (1), the wave function $|\Psi(t)\rangle$ is expanded in a discrete basis of the eigenstates of the field-free Hamiltonian $\hat{H}_0$ composed of the ground state ($k = 0$) and all the excited states ($k > 0$),

$$|\Psi(t)\rangle = \sum_{k\ge 0} c_k(t)|\Psi_k\rangle, \tag{4}$$

where $c_k(t)$ are time-dependent coefficients. Inserting Eq. (4) into Eq. (1), and projecting on the eigenstates $\langle\Psi_l|$, gives the evolution equation

$$i\frac{\partial\mathbf{c}(t)}{\partial t} = (\mathbf{H}_0 + \mathbf{V}(t))\mathbf{c}(t), \tag{5}$$

where $\mathbf{c}(t)$ is the column matrix of the coefficients $c_k(t)$, $\mathbf{H}_0$ is the diagonal matrix of elements, i.e., $\mathbf{H}_{0,lk} = \langle\Psi_l|\hat{H}_0|\Psi_k\rangle = E_k\delta_{lk}$ (where E_k is the energy of the eigenstate k), and $\mathbf{V}(t)$ is the non-diagonal matrix of elements, i.e., $\mathbf{V}_{lk}(t) = \langle\Psi_l|\hat{V}(t)|\Psi_k\rangle$. The initial wave function at $t = t_i = 0$ is chosen to be the field-free ground state, i.e., $c_k(t_i) = \delta_{k0}$. To solve Eq. (5), time is discretized and the split-propagator approximation is used, which reads as

$$\mathbf{c}(t+\Delta t) \approx e^{-i\mathbf{V}(t)\Delta t}e^{-i\mathbf{H}_0\Delta t}\mathbf{c}(t), \tag{6}$$

where Δt is the time step of the propagation. Since the matrix $\mathbf{H}_0$ is diagonal, $e^{-i\mathbf{H}_0\Delta t}$ is also a diagonal matrix of elements $e^{-iE_k\Delta t}\delta_{lk}$. The exponential of the non-diagonal matrix $\mathbf{V}(t)$ is calculated as

$$e^{-i\mathbf{V}(t)\Delta t} = \mathbf{U}^\dagger\, e^{-i\mathbf{V}_\mathrm{d}(t)\Delta t}\,\mathbf{U}, \tag{7}$$

where $\mathbf{U}$ is the unitary matrix describing the change of basis between the original eigenstates of $\hat{H}_0$ and a basis in which $\hat{V}(t)$ is diagonal, i.e., $\mathbf{V}_\mathrm{d}(t) = \mathbf{U}\mathbf{V}(t)\mathbf{U}^\dagger$.[18,21]

Once the time-dependent wavefunction $|\Psi(t)\rangle$ is known, the time-dependent dipole $\boldsymbol{\mu}(t)$ is computed as

$$\boldsymbol{\mu}(t) = \sum_{lk} c_l^*(t)c_k(t)\langle\Psi_l|\hat{\boldsymbol{\mu}}|\Psi_k\rangle \tag{8}$$

from which, by taking the Fourier transform, the HHG spectrum is obtained,

$$P(\omega) = \left|\sum_{lk}\langle\Psi_l|\hat{\boldsymbol{\mu}}|\Psi_k\rangle\frac{1}{t_f - t_i}\int_{t_i}^{t_f} W(t)c_l^*(t)c_k(t)e^{-i\omega t}dt\right|^2, \tag{9}$$

where t_i and t_f are the initial and final propagation times and $W(t)$ is the Hann (or Hanning) window function.

In the present work, we considered in Eq. (4), as truncated basis set, the molecular excited states described at the CIS and TDDFT level of theory. The extension of this approach to the solution of the TDSE in the presence of a strong field brings to the RT-TD-CIS and RT-TDDFT methods that will be described in the following.

A. RT-TD-CIS

RT-TD-CIS is the time-dependent extension of the CIS method.[51] In RT-TD-CIS, the time-dependent wave function is written on the truncated eigenstate basis of the CIS wave functions,

$$|\Psi(t)\rangle = \sum_{k=0} c_k(t)|\Psi_k^{\mathrm{CIS}}\rangle. \tag{10}$$

$|\Psi_k^{\mathrm{CIS}}\rangle$ are constructed by applying the excitation operator $\hat{R} = r_0 + \sum_{ia} r_i^a\hat{a}_a^\dagger\hat{a}_i$ on the Hartree–Fock (HF) description of the field-free system, i.e., $|\Psi_k^{\mathrm{CIS}}\rangle = \hat{R}_k|\phi_0^{\mathrm{HF}}\rangle$. Here and throughout this paper, we use the indices i and j for occupied orbitals, a and b for virtual ones, and p for generic orbitals. The operators $\hat{a}_p^\dagger$ and $\hat{a}_p$ create and annihilate an electron in the orbital $|\phi_p\rangle$, and the amplitudes r_0 and r_i^a are determined by solving the secular equation $\mathbf{AX} = \omega^{\mathrm{CIS}}\mathbf{X}$, where $\omega^{\mathrm{CIS}} = E^{\mathrm{CIS}} - E_0^{\mathrm{HF}}$ is the diagonal matrix of the excitation energies and $\mathbf{X}$ is the matrix of the CIS amplitudes (r_0, r_i^a). E_0^{HF} is the HF ground-state energy. The amplitude r_i^a refers to the Slater determinant associated with the promotion of a single orbital from the occupied orbital i to the virtual a, while r_0 is the CIS amplitude of the HF configuration. The matrix elements of $\mathbf{A}$ are given by

$$A_{ia,jb} = (\epsilon_a^{\mathrm{HF}} - \epsilon_i^{\mathrm{HF}})\delta_{ij}\delta_{ab} + \langle aj|w_{\mathrm{ee}}|ib\rangle - \langle aj|w_{\mathrm{ee}}|bi\rangle, \tag{11}$$

where $w_{\mathrm{ee}}(r) = 1/r$ is the Coulomb electron–electron interaction (with r being the distance between two electrons), $\langle aj|w_{\mathrm{ee}}|ib\rangle$ is the two-electron integral associated with the direct Coulomb, and $\langle aj|w_{\mathrm{ee}}|bi\rangle$ is the two-electron integral associated with the Coulomb exchange. The energies ϵ_i^{HF} (ϵ_a^{HF}) are the HF occupied-(virtual-) orbital energies, and i, j and a, b refer to the occupied and virtual HF orbitals, respectively.

B. RT-TDDFT

The time-dependent wave function can be formally expanded in the field-free linear-response TDDFT states,

$$|\Psi(t)\rangle = \sum_{k=0} c_k(t) \left|\Psi_k^{\mathrm{TDDFT}}\right\rangle. \tag{12}$$

As for CIS, the $|\Psi_k^{\mathrm{TDDFT}}\rangle$ can be constructed by applying the excitation operator $\hat{R}$ on the KS ground-state Slater determinant of the field-free system, i.e., $|\Psi_k^{\mathrm{TDDFT}}\rangle = \hat{R}_k|\phi_0^{\mathrm{KS}}\rangle$.

Within the Tamm–Dancoff approximation (TDA), the TDDFT amplitudes are determined by solving $\mathbf{AX} = \omega^{\mathrm{TDDFT/TDA}}\mathbf{X}$, where in this case, $\omega^{\mathrm{TDDFT/TDA}} = E^{\mathrm{TDDFT/TDA}} - E_0^{\mathrm{KS}}$ is the diagonal matrix of the excitation energies. E_0^{KS} is the KS ground-state energy.

In the adiabatic approximation, the matrix elements of $\mathbf{A}$ are given by

$$A_{ia,jb} = (\epsilon_a^{\mathrm{KS}} - \epsilon_i^{\mathrm{KS}})\delta_{ij}\delta_{ab} + \langle aj|w_{\mathrm{ee}}|ib\rangle + \langle aj|f_{\mathrm{x}}^{\mathrm{DFT}}|ib\rangle + \langle aj|f_{\mathrm{c}}^{\mathrm{DFT}}|ib\rangle, \tag{13}$$

where ϵ_i^{KS} and ϵ_a^{KS} are the KS energies of occupied and virtual orbitals, $\langle aj|w_{\mathrm{ee}}|ib\rangle$ is the two-electron integral associated with the direct Coulomb, and $\langle aj|_{\mathrm{x}}^{\mathrm{DFT}}|ib\rangle$ and $\langle aj|f_{\mathrm{c}}^{\mathrm{DFT}}|ib\rangle$ are, respectively, the DFT exchange and correlation integrals, which can be calculated in different density functional approximations. In this work, we used for $f_{\mathrm{xc}}^{\mathrm{DFT}}$ the PBE functional, and its extension in real time will be labeled RT-TD-PBE.

When the range-separation approach is used, the matrix element $A_{ia,jb}$ in Eq. (13) becomes

$$\begin{aligned} A_{ia,jb} = {} & (\epsilon_a^{\mathrm{KS}} - \epsilon_i^{\mathrm{KS}})\delta_{ij}\delta_{ab} + \langle aj|w_{\mathrm{ee}}|ib\rangle + \langle aj|f_{\mathrm{x}}^{\mathrm{lr},\omega,\mathrm{HF}}|ib\rangle \\ & + \langle aj|f_{\mathrm{x}}^{\mathrm{sr},\omega,\mathrm{DFT}}|ib\rangle + \langle aj|f_{\mathrm{c}}^{\mathrm{DFT}}|ib\rangle, \end{aligned} \tag{14}$$

where $\langle aj|f_{\mathrm{x}}^{\mathrm{lr},\omega,\mathrm{HF}}|ib\rangle = -\langle aj|w_{\mathrm{ee}}^{\mathrm{lr},\omega}|bi\rangle$ is the HF long-range Coulomb exchange and $\langle aj|f_{\mathrm{x}}^{\mathrm{sr},\omega,\mathrm{DFT}}|ib\rangle$ is the short-range DFT Coulomb exchange. In the integrals, we explicitly indicated the dependence on the parameter ω, which controls the range-separation of the Coulomb electron–electron interaction. In this work, we used the LC-ωPBE scheme where the kernel is $f_{\mathrm{xc}}^{\text{LC-}\omega\mathrm{PBE}} = f_{\mathrm{x}}^{\mathrm{lr},\omega,\mathrm{HF}} + f_{\mathrm{x}}^{\mathrm{sr},\omega,\mathrm{DFT}} + f_{\mathrm{c}}^{\mathrm{DFT}}$. For $\omega = 0$, the scheme reduces to the usual linear-response TDDFT/TDA as in Eq. (13) in PBE. For $\omega = \infty$, the scheme reduces to CIS plus PBE correlation (PBEc). The extension in real time will be labeled RT-TD-LC-ωPBE.

III. COMPUTATIONAL METHODS

In RT-TD-CIS and RT-TDDFT (RT-TD-PBE or RT-TD-LC-ωPBE), the time-dependent wavefunction is expanded using a finite number of electronic excited states and transition dipole moments from the corresponding frequency-domain methods: CIS and TDDFT (PBE or LC-ωPBE). In the case of the LC-ωPBE functional, we used the range-separation parameter $\omega = 0.3$ and $\omega = 0.4$, following Refs. 49 and 60. Moreover, in order to decouple the effect of exchange and correlation, we also calculated the CIS plus PBE correlation (CIS+PBEc) by adding the $\langle aj|f_{\mathrm{c}}^{\mathrm{DFT}}|ib\rangle$ term in Eq. (11), PBE only with exchange (PBEx) and LC-ωPBE only with exchange (LC-ωPBEx), and by removing the $\langle aj|f_{\mathrm{c}}^{\mathrm{DFT}}|ib\rangle$ term from Eq. (13) and Eq. (14).

These frequency-domain methods propagated in time are labeled RT-TD-CIS+PBEc, RT-TD-PBEx, and RT-TD-LC-ωPBEx (with $\omega = 0.3$ or 0.4). The TDDFT calculations were done within TDA. The dipole matrix elements were taken from field-free calculations by means of the Q-Chem software package[70] and employed in an homemade code, Light,[18,20,21,47,71] that propagates the wavepacket under the influence of a time-dependent strong field.

For all the theoretical methods employed, we used the computational strategy we developed in the recent years, which demonstrated to be successful to describe HHG for atomic[21,54,72] and small molecular species.[19,47] We combined Gaussian continuum functions (K) with the double-d heuristic lifetime model.[19,21,54,72,73] This model prevents unphysical reflections of the wave function in the laser-driven dynamics. The heuristic lifetime model was originally proposed by Klinkusch *et al.*,[73] and it consists of adding to the energies calculated from the field-free Hamiltonian an imaginary term $\Gamma_k = \sum_{ia} |r_{i,k}^a|^2 \sqrt{2\epsilon_a^{\mathrm{HF/KS}}}/d$ ($\epsilon_a^{\mathrm{HF/KS}} > 0$), which represents the inverse lifetime. This approach is developed within singly excited schemes.[22] The parameter d is empirical, representing the characteristic escape length that the electron is allowed to travel during the lifetime $1/\Gamma_k$. Recently, we extended this model to two parameters (double-d heuristic lifetimes).[19,21,54,72] These parameters are chosen on the basis of the three-step model.[12,13] d_0 is equal to the maximum electron excursion after ionization while $d_1 < d_0$. Moreover, d_0 affects all the continuum states below the cutoff energy $1.32I_p + 3.17U_p$ (I_p is the ionization potential energy and U_p is the ponderomotive energy), while d_1 affects all the continuum states above the cutoff energy. The parameter d_1 is especially chosen to remove high-lying above-threshold states.[19,21,54,72]

We used the following Gaussian basis sets with K functions: 6aug-cc-pVTZ+6K for H_2, 6aug-cc-pVTZ+3K for N_2, and 6aug-cc-pVDZ+6K for CO_2. The basis sets are reported in the supplementary material.

All results correspond to electronic dynamics at fixed nuclear geometries. To enable uniform comparison of the electron dynamics, we performed all calculations at the experimental equilibrium distance of 1.400 a_0 for H_2, 2.074 a_0 for N_2, and 2.209 a_0 for CO_2.

We computed HHG spectra for a $\cos^2$-shaped laser field [see Eq. (3)] with carrier frequency $\omega_0 = 0.057$ hartree (1.55 eV, 800 nm) and intensity $I = 10^{14}$ W/cm^2 ($d_0 = 16.478$ a_0 and $d_1 = 1.414$ a_0). In parentheses, we reported the values of the escape length parameters used for the heuristic lifetime model. The laser was linearly polarized both perpendicular and parallel to the molecular axis. The duration of the pulse was 20 optical cycles (oc) ($\sigma = 20$ oc), where 1 oc $= 2\pi/\omega_0$. The time step was 0.24 as (0.01 a.u.).

In Table I, we reported the molecular cutoff calculated as $(1.32I_p + 3.17U_p)/\omega_0$.[12,13] The cutoff energy gives an indication of the maximum photon energy in the harmonic spectrum, and it is one of the most important features of any HHG spectrum. In fact, the spectrum is composed of three parts: a perturbative region, where the intensity of the harmonics produced decreases rapidly, a "plateau" region, where the intensity of the harmonics is almost constant, and a cutoff region, where

TABLE I. Cutoff for the HHG spectrum with I = 10^{14} W/cm^2.

	H_2	N_2	CO_2
RT-TD-CIS	25.92	30.20	30.76
RT-TD-CIS+PBEc	31.11	31.11	31.73
RT-TD-LC-ωPBEx (ω = 0.4)	24.44	27.22	27.47
RT-TD-LC-ωPBE (ω = 0.4)	25.06	28.07	28.40
RT-TD-LC-ωPBEx (ω = 0.3)	23.76	26.38	26.64
RT-TD-LC-ωPBE (ω = 0.3)	24.37	27.22	27.54
RT-TD-PBEx	20.41	22.82	23.07
RT-TD-PBE	18.85	23.65	23.97

TABLE II. Ionization potential energy (I_p) in Hartree for the different theoretical schemes. Experimental values are also reported. In parentheses, we also reported the number of bound states, i.e., below the I_p, and of the number of continuum states, i.e., above the I_p, used in the time-dependent propagation.

	H_2	N_2	CO_2
I_p^{CIS}	0.594 (76/126)	0.779 (543/458)	0.803 (788/712)
$I_p^{CIS+PBEc}$	0.623 (78/124)	0.818 (543/460)	0.845 (797/704)
$I_{p\ \omega=0.4}^{LC\text{-}\omega PBEx}$	0.530 (76/126)	0.650 (512/489)	0.661 (797/704)
$I_{p\ \omega=0.4}^{LC\text{-}\omega PBE}$	0.557 (76/126)	0.687 (513/488)	0.701 (748/752)
$I_{p\ \omega=0.3}^{LC\text{-}\omega PBEx}$	0.501 (76/126)	0.614 (507/494)	0.625 (740/761)
$I_{p\ \omega=0.3}^{LC\text{-}\omega PBE}$	0.527 (76/126)	0.650 (507/494)	0.664 (742/758)
I_p^{PBEx}	0.356 (9/193)	0.460 (330/671)	0.471 (529/972)
I_p^{PBE}	0.381 (0/202)	0.496 (329/672)	0.510 (543/957)
I_p^{Exp}	0.567[74]	0.673[75]	0.711[76]

the intensity of the harmonics start to decrease until the signal goes out completely. The cutoff indicates that the extent of the HHG spectrum depends on the nature of the spectroscopic target, via I_p, and also on the intensity and wavelength of the laser, via U_p. In Table II, we also reported the I_p values at different levels of theory, together with the corresponding experimental ones. In the case of H_2, the I_p is minus the HOMO energy, for N_2 is minus the HOMO-2 energy, and for CO_2 is the HOMO-3 energy. The choice of the I_p for N_2 and CO_2 was motivated by the inclusion of all possible ionization channels that have been demonstrated participating in the electron dynamics generating the HHG spectrum. The HHG spectra of H_2, N_2, and CO_2 with the perpendicular pulse polarization are reported in the supplementary material.

IV. RESULTS AND DISCUSSION

In the following, we will attempt to answer the following question: how different theoretical descriptions of the electronic exchange and correlation can affect the shape of the HHG spectra of the H_2, N_2, and CO_2 molecular systems?

A. H_2

To understand the role of exchange and correlation in HHG for the H_2 molecule, we started to analyze the truncated basis composed

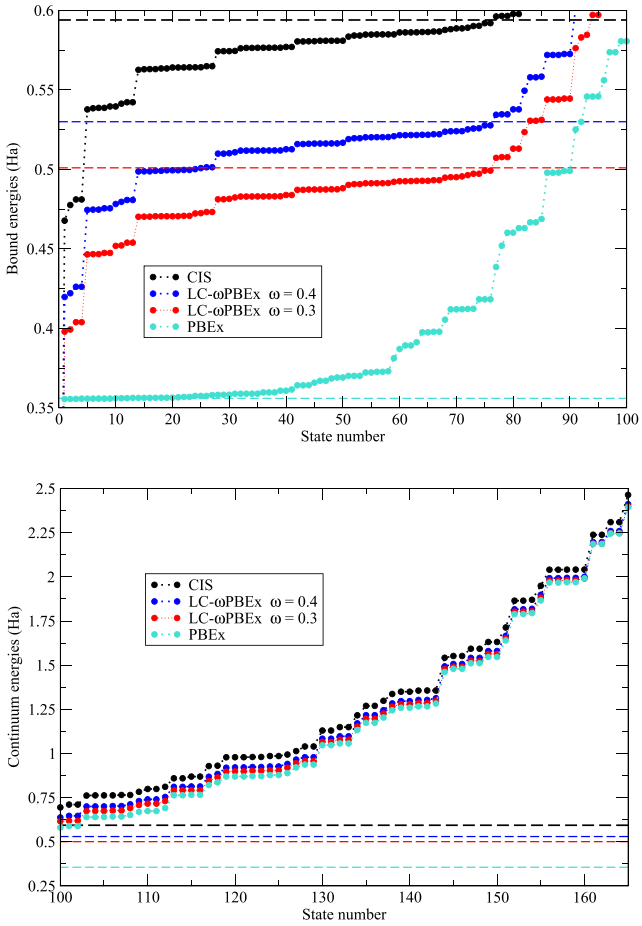

FIG. 1. H_2 excitation energies only with exchange: bound (top, states 0–100) and continuum (bottom, states 100–170) energies for CIS, LC-ωPBEx with ω = 0.3 and ω = 0.4, and PBEx. The I_p is also reported. The panels are a zoomed-in view of the energy region of interest for the calculated HHG spectra.

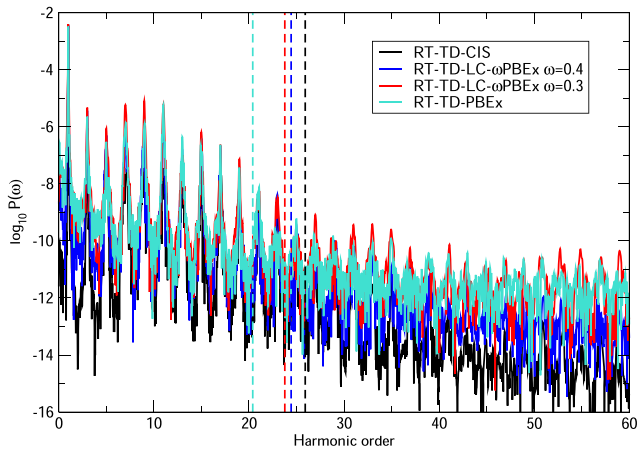

FIG. 2. H_2: HHG spectra only with exchange for RT-TD-CIS, RT-TD-LC-ωPBEx with ω = 0.3 and ω = 0.4, and RT-TD-PBEx. The laser has I = 10^{14} W/cm^2, ω = 0.057 hartree, and polarization parallel to the molecular axis.

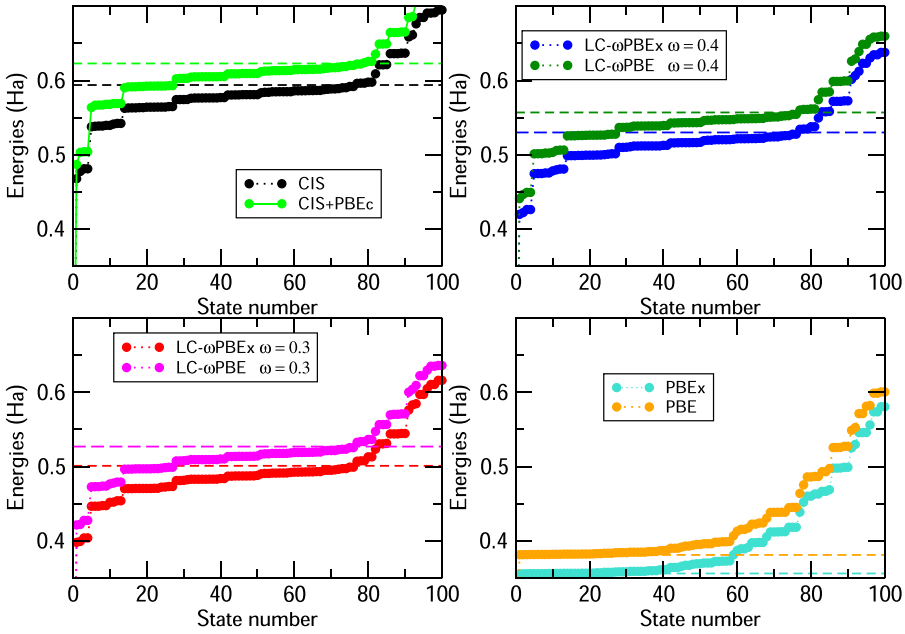

FIG. 3. H_2 excitation energies with exchange and correlation: bound and onset of continuum energies for CIS vs CIS+PBEc, LC-ωPBEx vs LC-ωPBE with ω = 0.3 and ω = 0.4, and PBEx vs PBE. The I_p is also reported.

of the ground- and excited-state correlated wave functions from the field-free Hamiltonian, which then define the time-dependent wavepacket in the RT-TD-CIS and in RT-TDDFT frameworks. In Fig. (1), we compared the bound and the continuum energy states of the truncated basis calculated by CIS, LC-ωPBEx (ω = 0.4 and ω = 0.3), and PBEx. This comparison takes into account only the exchange contribution.

CIS is considered as the method of reference as it contains HF exchange with correct asymptotic behavior of the Coulomb potential $(-1/r)$. The comparison with the other methods was done by taking the HF ground state energy as the zero energy reference. In Fig. (1), for each theoretical methods, we also plotted the I_p (see Table II). In Table II, we also reported the number of bound and continuum states for each theoretical scheme.

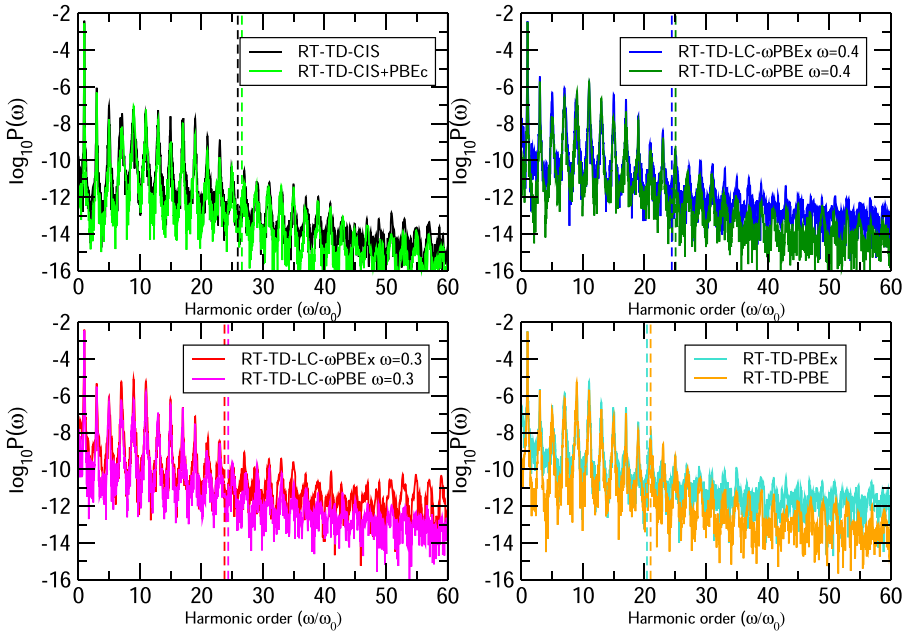

FIG. 4. H_2: HHG spectra for RT-TD-CIS vs RT-TD-CIS+PBEc, RT-TD-LC-ωPBEx vs RT-TD-LC-ωPBE with ω = 0.3 and ω = 0.4, and RT-TD-PBEx vs RT-TD-PBE. The laser has I = 10^{14} W/cm^2, ω = 0.057 hartree, and polarization parallel to the molecular axis.

Considering the top panel of Fig. (1), we observe that the CIS methods satisfactorily represent the Rydberg states because of the correct asymptotic behavior of the Coulomb potential. The I_p in CIS (Table II) also has the best agreement with the experimental value compared to the other theoretical schemes. Considering PBEx, for which the Coulomb potential decays exponentially at large distances, we observe that it does not support the Rydberg series of bound states. In this case, the I_p has the worst agreement with the experimental value when compared to the other theoretical calculations. This behavior is also supported by comparing the number of bound states of PBEx in Table II with the other theoretical methods: the number of computed PBEx bound states is considerably lower. This is consistent with the wrong asymptotic behavior of the Coulomb exchange potential of PBEx.

The LC-ωPBEx contains a percentage of the HF long-range exchange and of the short-range PBE exchange. In the limit of $\omega = \infty$, the LC-ωPBEx scheme reduces to CIS, while for $\omega = 0$, the LC-ωPBEx scheme reduces to the PBEx. Therefore, by construction, the LC-ωPBEx with $\omega = 0.4$ and $\omega = 0.3$ connects the CIS and the PBEx schemes. Considering $\omega = 0.4$, the excitation energies are closer to the CIS, while for $\omega = 0.3$, the excitation energies are closer to the PBEx. The corresponding I_p values in Table II reflect the same behavior.

In the bottom panel of Fig. (1), the continuum energy states are compared. The trend is similar to the one observed for the bound states (top panel). However, despite the energy shift between the different methods, the continuum energy density is the same for all the theoretical schemes.

The bound and continuum energy states represented in Fig. (1) are also the energy space in which the electrons move during the propagation, which can affect the description of the HHG spectrum. In Fig. (2), we show how these different electronic-structure descriptions impact the HHG spectrum of H_2. For each level of theory, we also plotted the molecular energy cutoff[12,13,19] reported in Table I.

RT-TD-CIS, with the 6aug-ccpVTZ+6K basis set, reproduces well the main features of a HHG spectrum: perturbative/plateau, cutoff, and background regions.[19,47] It is interesting to compare this spectrum with other RT-TD-CIS calculations, which used different basis sets. Luppi and Head-Gordon[18] calculated the HHG spectrum for H_2 using various Gaussian basis sets, the largest one being d-aug-cc-pVTZ. The general trend of the HHG spectrum with this basis set is correct. However, for the region just beyond the cutoff, the comparison with the 6aug-cc-pVTZ+6K basis set shows some differences due to the lack of diffuse functions and optimized K functions for the continuum states.

The HHG spectrum in RT-TD-CIS of the H_2 molecule was also calculated by White *et al.*[47] using the 6aug-cc-pVTZ and the 6aug-cc-pVTZ with additional basis function centers (ghost atoms). The 6aug-cc-pVTZ and 6aug-cc-pVTZ+6K give the same spectrum up to the 25th harmonic. Next, the lack of optimized Gaussian functions for continuum makes appear in the 6aug-cc-pVTZ a number of extra (artificial) harmonics, which are due to diffuseness of the basis set.

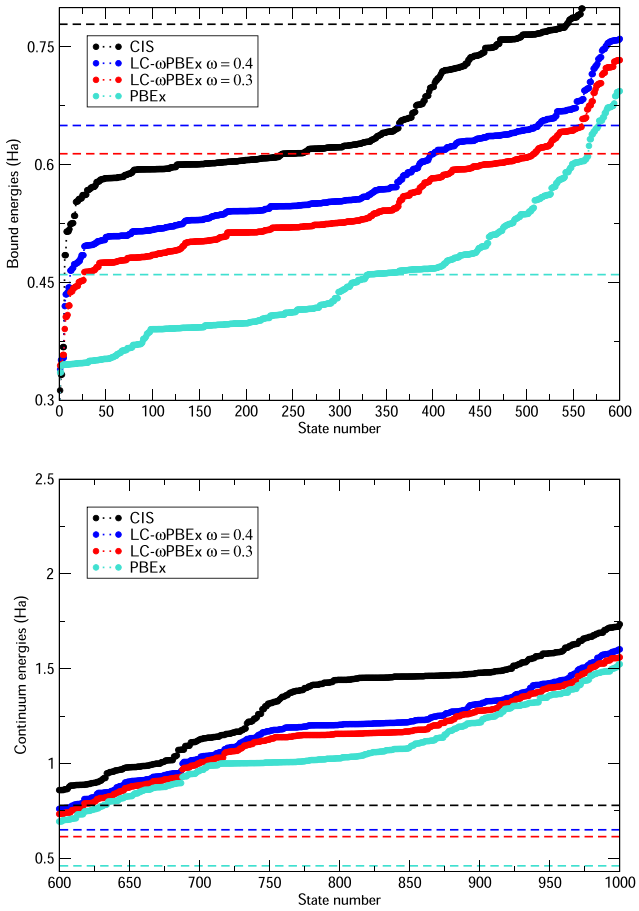

FIG. 5. N_2 excitation energies only with exchange: bound (top, states 0–600) and continuum (bottom, states 600–1000) energies for CIS, LC-ωPBEx with $\omega = 0.3$ and $\omega = 0.4$, and PBEx. The I_p is also reported. The panels are a zoomed-in view of the energy region of interest for the calculated HHG spectra.

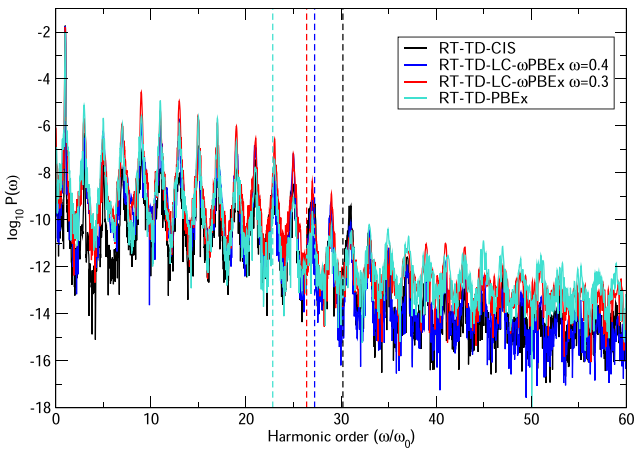

FIG. 6. N_2: HHG spectra only with exchange for RT-TD-CIS, RT-TD-LC-ωPBEx with $\omega = 0.3$ and $\omega = 0.4$, and RT-TD-PBEx. The laser has $I = 10^{14}$ W/cm^2, $\omega = 0.057$ hartree, and polarization parallel to the molecular axis.

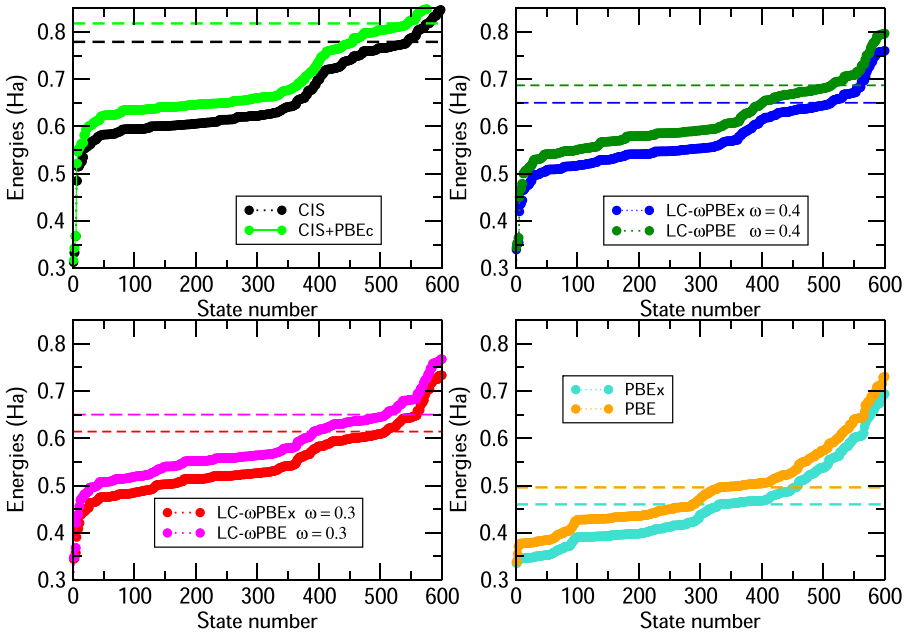

FIG. 7. N_2 excitation energies with exchange and correlation: bound and onset of continuum energies for CIS vs CIS+PBEc, LC-ωPBEx vs LC-ωPBE with ω = 0.3 and ω = 0.4, and PBEx vs PBE. The I_p is also reported.

For this reason, White *et al.*[47] found a second plateau, which is much more pronounced than what we found with the 6aug-cc-pVTZ+6K basis set.

The other approach used by White *et al.*[47] to correct their basis for the continuum states was to insert ghost atoms in different geometrical configurations around the H_2 molecule. This technique permits to make disappear some of the spurious harmonics at high energy. Using this strategy makes the second plateau less evident than with 6aug-cc-pVTZ, which is more in agreement with what we found with the 6aug-cc-pVTZ+6K basis set. Comparison between the effects from ghost atoms and K functions is also reported for the HHG spectrum of the hydrogen atom in Ref. 20.

The differences between our HHG spectrum and the one calculated by White *et al.*[47] with ghost atoms can also be due to the different approach to treat ionization during the propagations. White

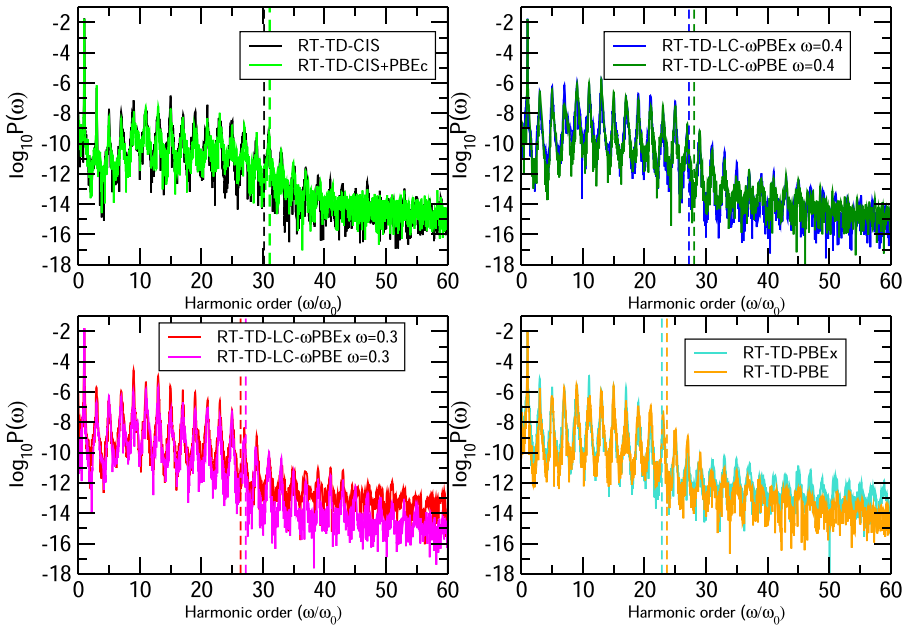

FIG. 8. N_2: HHG spectra for RT-TD-CIS vs RT-TD-CIS+PBEc, RT-TD-LC-ωPBEx vs RT-TD-LC-ωPBE with ω = 0.3 and ω = 0.4, and RT-TD-PBEx vs RT-TD-PBE. The laser has I = 10^{14} W/cm^2, ω = 0.057 hartree, and polarization parallel to the molecular axis.

et al.[47] used a heuristic lifetime model with only one escape length, at variance with what was done by us in this work (Sec. III). This means that the two HHG spectra differently exclude some recombination processes, which proceed through continuum states, including some classes of long-lived resonances.

In Fig. (2), we also report the HHG spectra computed by means of other theoretical approaches. The RT-TD-LC-ωPBEx with ω = 0.4 is the closest approach to RT-TD-CIS considering the description of the exchange. In fact, it contains a large percentage of HF exchange and a small percentage of PBE exchange. The effect is an overall increase in the spectrum intensity. The second plateau almost disappears. The RT-TD-LC-ωPBEx with ω = 0.3 has a higher percentage of the PBEx with respect to ω = 0.4. In addition, in this case, the spectrum intensity is generally increased with respect to RT-TD-CIS. However, some harmonics reappear at higher energy. Considering the HHG in PBEx, we observe that the peak intensities in the plateau region are not forcefully higher than with RT-TD-LC-ωPBEx with ω = 0.3, but the peaks are certainly more noisy. The most important feature with PBEx is that no second plateau is described. Some harmonics are very badly reproduced or not even resolved.

To go further with our analysis, we include the role of the PBE correlation (PBEc). In Fig. (3), we show the bound and the onset of the continuum energy states calculated by CIS+PBEc, LC-ωPBE (ω = 0.3 and ω = 0.4), and PBE. The effect is the same for all the theoretical schemes. We obtain a rigid shift of the excitation energies and also of the I_p (see Table II). It is interesting to note that for the PBE, we found no bound states.

In Fig. (4), we analyzed the HHG for H_2 by comparing the theoretical schemes with only exchange to the same schemes where we also included the PBEc. In the case of CIS, adding PBEc has very little impact. PBEc slightly lowers the intensity of some harmonics. Instead, PBEc has larger impact on LC-ωPBEx (ω = 0.3 and ω = 0.4) and PBEx. The harmonics in the plateau lower their intensities, but the strongest effect is shown for those harmonics in the region after the cutoff. PBEc seems to lower the background and therefore to better resolve high energy harmonics. Moreover, RT-TD-LC-ωPBE and RT-TDPBE are closer to RT-TD-CIS when PBEc is included. This behavior can be attributed to a compensation effect between the short-range PBEx and PBEc.

B. N_2

To understand the role of exchange and correlation in HHG for the N_2 molecule, we compared in Fig. (5) the bound and the continuum energy states calculated by CIS, LC-ωPBEx (ω = 0.4 and ω = 0.3), and PBEx. These are the energies of the truncated basis used in the RT-TD-CIS and in RT-TDDFT calculations. In Fig. (5), we also plotted the I_p (see Table II) for the different levels of theory. We remind that in this case, I_p is calculated as minus the HOMO-2 energy. As in the case of the H_2 molecule, the CIS method is our reference because of the correct asymptotic behavior of the electron Coulomb potential.

In the top panel of Fig. (5), the CIS shows a large number of bound states below the I_p. The behavior of the other theoretical approaches follows the same trend observed for the H_2 molecule. The plateau structures below I_p indicate the presence of other ionization channels, related to electron ionization from HOMO and HOMO-1. In the bottom panel of Fig. (5), the continuum energy states are compared. The trend is similar to the one observed for the bound states (top panel) but less regular than the trend for the continuum of the H_2 molecule.

In Fig. (6), we show the HHG spectra for the different theoretical schemes only including the electron exchange. The general trend already observed in H_2 is reproduced also for N_2. HHG peaks by RT-TD-PBEx are slightly more intense and also more noisy than those described by RT-TD-CIS. The RT-TD-LC-ωPBEx with ω = 0.3 behaves close to RT-TD-PBEx, while RT-TD-LC-ωPBEx with ω = 0.4 is similar to RT-TD-CIS.

Luppi and Head-Gordon[18] calculated the HHG spectrum of N_2 in RT-TD-CIS with different Gaussian basis sets. The largest one was the d-aug-cc-pVTZ. From the comparison with our results, obtained with the 6aug-cc-pVTZ+3K basis set, we observe a similar behavior of the two chosen computational protocols. However, we confirm that as for the H_2 molecule, the critical point is the description of the energy region around the cutoff. The cutoff region

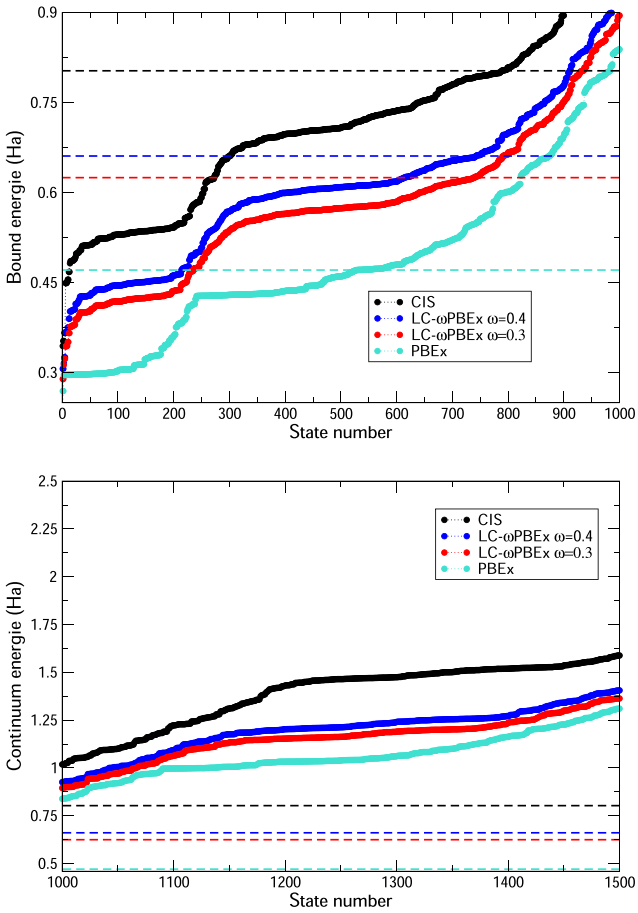

FIG. 9. CO_2 excitation energies only with exchange: bound (top, states 0–1000) and continuum (bottom, states 1000–1500) energies for CIS, LC-ωPBEx with ω = 0.3 and ω = 0.4, and PBEx. The I_p is also reported. The panels are a zoomed-in view of the energy region of interest for the calculated HHG spectra.

is poorly described by the d-aug-cc-pVTZ basis sets, which lacks a (large) number of diffuse functions and optimized K functions for the continuum states.

To go further in our analysis, we include the role of the PBE correlation (PBEc). In Fig. (7), we show the bound and the onset of the continuum energy states calculated by CIS+PBEc, LC-ωPBE (ω = 0.3 and ω = 0.4), and PBE. The effect is the same for all the theoretical schemes. We obtain a rigid shift of the excitation energies and of the I_p (see Table II).

In Fig. (8), we analyzed the HHG for N_2 by comparing the theoretical schemes with only exchange to the same schemes where we also included the PBEc term. In the case of RT-TD-CIS, adding PBEc has very little impact. PBEc slightly lowers the intensity of some harmonics. Instead, PBEc has larger impact on RT-TD-LC-ωPBEx (ω = 0.3 and ω = 0.4) and RT-TD-PBEx. The harmonics in the plateau lower their intensities, but the strongest effect is shown for those harmonics in the region after the cutoff. PBEc seems to lower the background and therefore to better resolve high energy harmonics. As for H_2, RT-TD-LC-ωPBE and RT-TD-PBE are characterized by a better agreement with RT-TD-CIS when the PBE correlation is included.

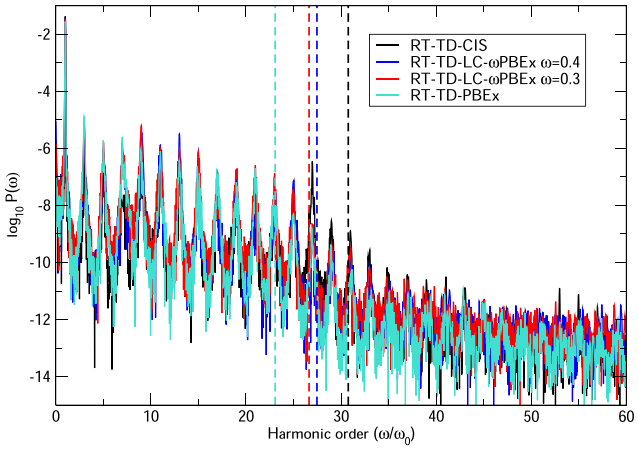

FIG. 10. CO_2: HHG spectra only with exchange for RT-TD-CIS, RT-TD-LC-ωPBEx with ω = 0.3 and ω = 0.4, and RT-TD-PBEx. The laser has I = 10^{14} W/cm^2, ω = 0.057 hartree, and polarization parallel to the molecular axis.

C. CO_2

In Fig. (9), we show the bound and the continuum energy states calculated by CIS, LC-ωPBEx (ω = 0.4 and ω = 0.3), and PBEx. These are the energies of the truncated basis used in the RT-TD-CIS and in RT-TDDFT schemes. In Fig. (9), we also plotted the I_p (see Table II) for the different levels of theory employed here. Again, the CIS description of the CO_2 electronic structure can be considered as a theoretical reference, thanks to the correct asymptotic behavior of the Coulomb potential.

In the top panel of Fig. (9), the behavior of the bound excitation energies, computed at the various levels of theory, is similar to the trend in H_2 and N_2. The PBEx largely underestimates the ionization threshold and therefore the continuum energy collapse, whereas increasing the HF character implies a better description of the long-range Coulomb potential and therefore of the bound excitation energies, which are then reproduced correctly together with the onset of the continuum. Another important observation is that in the case of CO_2, we observe energy plateau structures, which are due to the presence of other ionization channels,

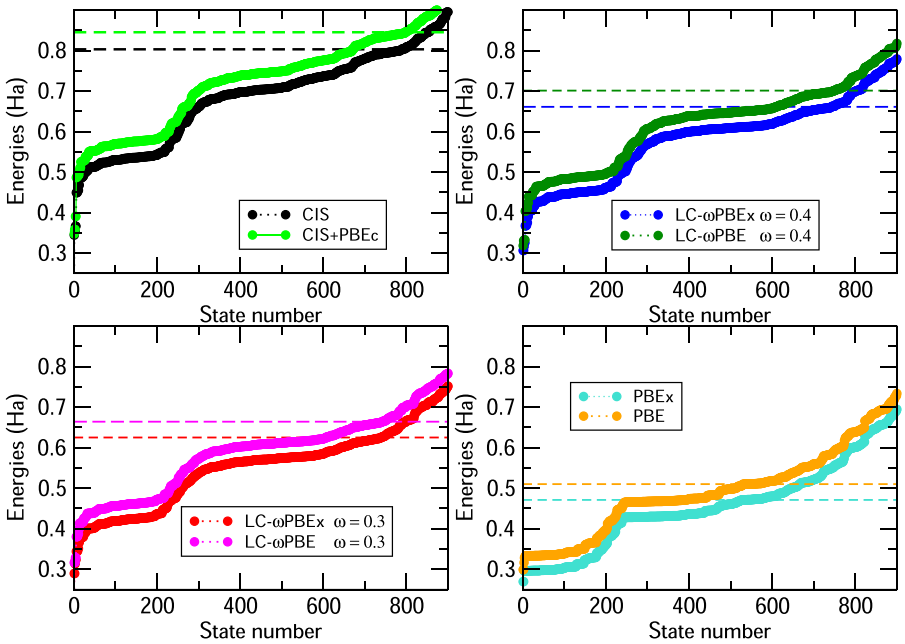

FIG. 11. CO_2 excitation energies with exchange and correlation: bound and onset of continuum energies for CIS vs CIS+PBEc, LC-ωPBEx vs LC-ωPBE with ω = 0.3 and ω = 0.4, and PBEx vs PBE. The I_p is also reported.

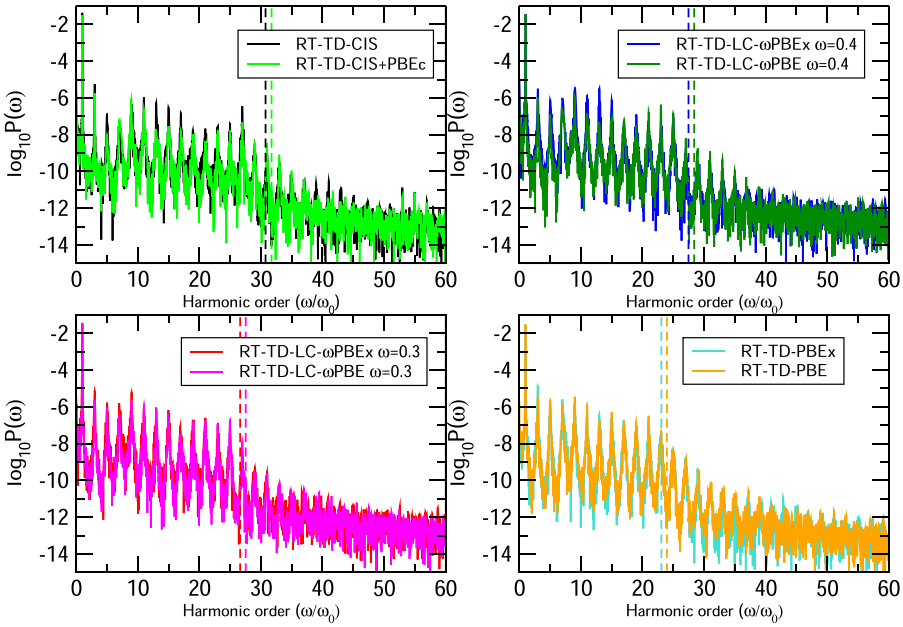

FIG. 12. CO_2: HHG spectra for RT-TD-CIS vs RT-TD-CIS+PBEc, RT-TD-LC-ωPBEx vs RT-TD-LC-ωPBE with ω = 0.3 and ω = 0.4, and RT-TD-PBEx vs RT-TD-PBE. The laser has I = 10^{14} W/cm^2, ω = 0.057 hartree, and polarization parallel to the molecular axis.

corresponding to the electron removal from HOMO, HOMO-1, and HOMO-2.

In the bottom panel of Fig. (9), the continuum energy states are compared for the different theoretical schemes. In addition, in this case, the trend is the same as in H_2 and N_2, the LC-ωPBEx energies with ω = 0.3 and 0.4 lie within the CIS and PBEx ones.

The effect of the different level of theory for electronic exchange and correlation employed to describe the CO_2 wavepacket, and therefore, the HHG spectra is shown in Fig. (10). RT-TD-CIS and RT-TD-LC-ωPBEx with ω = 0.3 and 0.4 have very similar behavior for the plateau, cutoff, and background region, except for very little differences in the peak intensity concerning the HHG in the plateau region, as already observed for H_2 and N_2. Instead, the behavior of RT-TD-PBEx is different. The intensity of the HHG spectrum is lower than with the other theoretical methods and, in particular, for the cutoff and background region. Moreover, it seems that harmonics continue to be present also at high energy, where instead the other methods do not describe any HHG anymore.

The effect of PBE correlation on top of the different theoretical schemes with only exchange is shown in Fig. (11) for the excitation energies. The behavior is consistent with the trend found for H_2 and N_2.

Including the correlation in the electronic-structure description does not produce any appreciable or systematic change in the HHG spectra, as shown in Fig. (12). The overall effect seems to be smaller than in H_2 and N_2 molecules.

D. Discussion

The physical mechanism at the origin of the HHG nonlinear process is usually described using the 3SM in which an electron is ionized by the laser pulse and subsequently driven far in the continuum by the laser field before finally recombining with the parent ion with the consequent emission of radiation. The 3SM relies on the single active electron (SAE) approximation, which supposes that it is only the outermost electron that contributes to the dynamics, while the other electrons are modeled by an effective potential. This implies that the electron correlation is not described and that the 3SM together with the SAE can only be qualitative.

For systems such as He where the correlation is small, the SAE can be a good approximation.[77] However, for atomic systems such as Be and Ne where the correlation is more important, it was necessary to go beyond the SAE and to use more accurate theoretical approaches.[27] In fact, using correlated methods permitted to describe for Be and Ne a second plateau well extended beyond the first one and also to identify a resonance peak above the plateau.[78] These features are a clear manifestation of electron correlation.[30]

In molecules, the description of the physics beyond the HHG spectroscopy is more complex than in atomic systems. In fact, together with the many-electron dynamics, there is also the possibility for the electrons to recombine with multiple atomic centers.[79] An indication of the role of electronic correlation was pointed out by finding a clear correspondence with multiple orbital contributions to some specific spectral features of HHG for N_2, O_2, CO_2, F_2, N_2O, and CO molecules.[24,66,67,80] Moreover, also for molecules, the many-electron dynamics brought evidence of a possible extension of the cutoff.[45]

Understanding how different theoretical schemes can describe the many-electron dynamics under the influence of a strong field, and therefore the HHG spectroscopy, becomes a fundamental task. We used RT-TD-CIS and RT-TDDFT approaches that propagate a truncated eigenstate basis with different flavors of the electron exchange, on which we added PBE correlation. These approaches demonstrated to reproduce accurate HHG spectra for H_2, N_2, and CO_2, but no large difference among the electronic-structure

descriptions was found. This implies that it is important to go beyond the SAE, but the HHG is not strongly sensitive to the way the electron exchange and correlation are treated. In the context of RT-TDDFT on a numerical grid, Chu and Memoli[45] compared the behavior of the exchange–correlation potential LB_α and of the local spin-density approximation with self-interaction correction (LSDA-SIC) to calculate HHG for the H_2 molecule. The exchange–correlation potentials are both corrected for the long-range behavior of the Coulomb potential. They found that the two methods reproduce very similar HHG, which is in agreement with what we have obtained.

A surprising observation by comparing the different methods is that RT-TD-PBE (and RT-TD-PBEx), which wrongly reproduces the asymptotic behavior of the Coulomb potential, gives HHG spectra rather similar to RT-TD-CIS and RT-TD-LC-ωPBEx ones. Some differences are present in the cutoff and background region, but they are very small. This would indicate that the wrong asymptotic behavior does not play a fundamental role (at least in our computational protocol). However, we want to point out that this result, which is also related to the self-interaction error, is still rather controversial.

Sun *et al.*[81] studied the molecular ion H_2^+. Their work focused on the numerical analysis of the self-interaction error in RT-TDDFT for H_2^+ which has just one electron. Through a comparison with the exact solution of the time-dependent Schrödinger (TDSE) for H_2^+, they showed that LDA and PBE are in agreement with the TDSE for the lowest part of the spectrum, but spurious harmonics appear at higher energy. They also studied the performance of the LB94 and of the Fermi–Amaldi scheme plus PBE (LFAsPBE), which have the correct asymptotic behavior of the Coulomb potential.[81] They found that LB94 and LFAsPBE are in better agreement with exact TDSE, i.e., the asymptotic behavior is important. However, they also found that LFAsPBE is better than LB94, implying that the fine details of the exchange and correlation potential also affect the HHG spectra.

Concerning the HHG of the N_2 molecule, Mack *et al.*[82] compared the LDA and LB94 exchange–correlation potential. Both the approaches can reproduce the main features of the HHG spectra. The LDA has slightly higher intensity, but it is still predictive and accurate. Chu and Chu[83] compared the HHG spectra of N_2 using the LSDA without self-interaction correction and LB_α and found 2–3 order of magnitude of difference in the spectra. Therefore, they pointed out the importance of incorporating the correct asymptotic long-range potential in the TDDFT treatment of strong field processes.[45]

Wardlow and Dundas[84] studied HHG in benzene, comparing LDA incorporating the Perdew–Wang parameterization of the correlation functional with and without self-interaction correction. The agreement between the two methods is very good. They observed an increase in the plateau harmonics and around the cutoff region, but for the method with the self-interaction correction.

The importance and the role of the long-range Coulomb potential and the electron exchange and correlation merit further theoretical investigations. The methods could have different sensitivity to the laser intensity and to the molecular systems. We believe the most critical point for all these methods is the description of the continuum and how it couples to the electron dynamics during the time-dependent propagation.

V. CONCLUSIONS

In this work, we studied the role of electronic exchange and correlation in the HHG spectroscopy of H_2, N_2, and CO_2 molecules using different *ab initio* electronic structures methods: RT-TD-CIS and RT-TDDFT (PBE and LC-ωPBE) using truncated basis sets composed of correlated wave functions from the corresponding field-free electronic Hamiltonian.

We computed HHG spectra for a $\cos^2$-shaped laser field with carrier frequency $\omega_0 = 0.057$ hartree (1.55 eV, 800 nm) and intensity $I = 10^{14}$ W/cm^2. We combined Gaussian continuum functions (K) and a heuristic lifetime model with two parameters for modeling ionization.[19,21,54,72]

We separated the effect of exchange from the effect of correlation by comparing the methods: RT-TD-CIS, RT-TD-LC-ωPBEx ($\omega = 0.3$ and $\omega = 0.4$), and RT-TD-PBEx, which contain only electronic exchange. This permitted, without any bias, to observe the effect of the long-range HF and of the short-range PBE on HHG. The correlation was then added in the form of PBE correlation.

All the methods give very similar HHG spectra, and they seem not to be particularly sensitive to the different description of exchange and correlation or to the correct asymptotic behavior of the Coulomb potential. Despite this general trend, some differences are found in the energy region connecting the cutoff and the background. Methods such as RT-TD-CIS, RT-TD-LC-ωPBEx ($\omega = 0.4$), and RT-TD-LC-ωPBE ($\omega = 0.4$), which contain long-range HF or at least a percentage of it, seem to better resolve the harmonics.

The investigation of electronic correlation in molecular HHG is a complex problem as the molecular continuum is coupled with strong field. This subject deserves further investigations, as, for example, the inclusion of double excitations and the analysis of other range-separated, hybrid and double-hybrid functionals.

SUPPLEMENTARY MATERIAL

See the supplementary material for the HHG spectra of H_2, N_2, and CO_2 for the different levels of theory, computed with a pulse polarization perpendicular to the molecular axis. Basis sets in the Q-Chem format are also reported.

ACKNOWLEDGMENTS

C.F.P. acknowledges the Extra Erasmus program of the University of Trieste and Sorbonne Universités for financial support. The authors acknowledge the Computational Center of the University of Trieste.

DATA AVAILABILITY

The data that support the findings of this study are available within the article and its supplementary material and from the corresponding author upon reasonable request.

REFERENCES

[1] G. Sansone, Nat. Photonics **14**, 131 (2020).
[2] A. J. Uzan *et al.*, Nat. Photonics **14**, 188 (2020).
[3] T. Gaumnitz *et al.*, Opt. Express **25**, 27506 (2017).
[4] C. Chappuis, D. Bresteau, T. Auguste, O. Gobert, and T. Ruchon, Phys. Rev. A **99**, 033806 (2019).

[5]A. Marciniak *et al.*, Nat. Commun. **10**, 337 (2019).
[6]P. Peng, C. Marceau, and D. M. Villeneuve, Nat. Rev. Phys. **1**, 144 (2019).
[7]M. Ossiander *et al.*, Nat. Phys. **13**, 280 (2017).
[8]R. Cireasa *et al.*, Nat. Phys. **11**, 654 (2015).
[9]M. Nisoli, P. Decleva, F. Calegari, A. Palacios, and F. Martín, Chem. Rev. **117**, 10760 (2017).
[10]J. P. Marangos, J. Phys. B: At., Mol. Opt. Phys. **49**, 132001 (2016).
[11]A. Dubrouil *et al.*, Nat. Commun. **5**, 4637 (2014).
[12]P. B. Corkum, Phys. Rev. Lett. **71**, 1994 (1993).
[13]M. Lewenstein, P. Balcou, M. Y. Ivanov, A. L'Huillier, and P. B. Corkum, Phys. Rev. A **49**, 2117 (1994).
[14]R. Santra and A. Gordon, Phys. Rev. Lett. **96**, 073906 (2006).
[15]A. Gordon, F. X. Kärtner, N. Rohringer, and R. Santra, Phys. Rev. Lett. **96**, 223902 (2006).
[16]S. Beaulieu *et al.*, Phys. Rev. Lett. **117**, 203001 (2016).
[17]F. Catoire *et al.*, Phys. Rev. Lett. **121**, 143902 (2018).
[18]E. Luppi and M. Head-Gordon, Mol. Phys. **110**, 909 (2012).
[19]M. Labeye *et al.*, J. Chem. Theory Comput. **14**, 5846 (2018).
[20]E. Coccia and E. Luppi, Theor. Chem. Acc. **135**, 43 (2016).
[21]E. Coccia *et al.*, Int. J. Quantum Chem. **116**, 1120 (2016).
[22]E. Coccia, R. Assaraf, E. Luppi, and J. Toulouse, J. Chem. Phys. **147**, 014106 (2017).
[23]J. Caillat *et al.*, Phys. Rev. A **71**, 012712 (2005).
[24]M. Ruberti, P. Decleva, and V. Averbukh, Phys. Chem. Chem. Phys. **20**, 8311 (2018).
[25]M. Nest, R. Padmanaban, and P. Saalfrank, J. Chem. Phys. **126**, 214106 (2007).
[26]T. Sato and K. L. Ishikawa, Phys. Rev. A **91**, 023417 (2015).
[27]T. Sato *et al.*, Phys. Rev. A **94**, 023405 (2016).
[28]M. C. H. Wong, J.-P. Brichta, M. Spanner, S. Patchkovskii, and V. R. Bhardwaj, Phys. Rev. A **84**, 051403(R) (2011).
[29]F. Bedurke, T. Klamroth, P. Krause, and P. Saalfrank, J. Chem. Phys. **150**, 234114 (2019).
[30]I. Tikhomirov, T. Sato, and K. L. Ishikawa, Phys. Rev. Lett. **118**, 203202 (2017).
[31]P. Krause, T. Klamroth, and P. Saalfrank, J. Chem. Phys. **123**, 074105 (2005).
[32]C. Huber and T. Klamroth, Appl. Phys. A **81**, 93 (2005).
[33]P. Krause, T. Klamroth, and P. Saalfrank, J. Chem. Phys. **127**, 034107 (2007).
[34]N. Rohringer, A. Gordon, and R. Santra, Phys. Rev. A **74**, 043420 (2006).
[35]T. Sato and K. L. Ishikawa, Phys. Rev. A **88**, 023402 (2013).
[36]N. Tancogne-Dejean *et al.*, J. Chem. Phys. **152**, 124119 (2020).
[37]T. P. Rossi, M. Kuisma, M. J. Puska, R. M. Nieminen, and P. Erhart, J. Chem. Theory Comput. **13**, 4779 (2017).
[38]P. Wopperer, P. M. Dinh, P.-G. Reinhard, and E. Suraud, Phys. Rep. **562**, 1 (2015).
[39]C.-Z. Gao, P. M. Dinh, P.-G. Reinhard, and E. Suraud, Phys. Chem. Chem. Phys. **19**, 19784 (2017).
[40]M. Vincendon, L. Lacombe, P. M. Dinh, E. Suraud, and P. G. Reinhard, Comput. Mater. Sci. **138**, 426 (2017).
[41]J. Pilmè, E. Luppi, J. Berés, C. Hoée-Levin, and A. de la Lande, J. Mol. Modell. **20**, 2368 (2014).
[42]X. Wu *et al.*, J. Chem. Theory Comput. **13**, 3985 (2017).
[43]X. Wu, A. Alvarez-Ibarra, D. R. Salahub, and A. de la Lande, Eur. J. Phys. D **72**, 206 (2018).
[44]A. Parise *et al.*, J. Phys. Chem. Lett. **9**, 844 (2018).
[45]X. Chu and P. J. Memoli, Chem. Phys. **391**, 83 (2011).
[46]F. Ding, W. Liang, C. T. Chapman, C. M. Isborn, and X. Li, J. Chem. Phys. **135**, 164101 (2011).
[47]A. F. White, C. J. Heide, P. Saalfrank, M. Head-Gordon, and E. Luppi, Mol. Phys. **114**, 947 (2016).
[48]J. A. Sonk, M. Caricato, and H. B. Schlegel, J. Phys. Chem. A **115**, 4678 (2011).
[49]J. A. Sonk and H. B. Schlegel, J. Phys. Chem. A **115**, 11832 (2011).
[50]M. E. Casida, "Time-dependent density functional response theory for molecules," in *Recent Advances in Density Functional Methods*, edited by D. P. Chong (World Scientific, Singapore, 1995), Part I, p. 155.
[51]A. Dreuw and M. Head-Gordon, Chem. Rev. **105**, 4009 (2005).
[52]T. Sato, H. Pathak, Y. Orimo, and K. L. Ishikawa, J. Chem. Phys. **148**, 051101 (2018).
[53]H. Pathak, T. Sato, and K. L. Ishikawa, J. Chem. Phys. **152**, 124115 (2020).
[54]E. Coccia and E. Luppi, Theor. Chem. Acc. **138**, 96 (2019).
[55]E. Runge and E. K. U. Gross, Phys. Rev. Lett. **52**, 997 (1984).
[56]E. K. U. Gross and W. Kohn, Phys. Rev. Lett. **55**, 2850 (1985).
[57]P. Elliott, S. Goldson, C. Canahui, and N. T. Maitra, Chem. Phys. **391**, 110 (2011).
[58]J. P. Perdew, Chem. Phys. Lett. **64**, 127 (1979).
[59]J. P. Perdew and A. Zunger, Phys. Rev. B **23**, 5048 (1981).
[60]O. A. Vydrov and G. E. Scuseria, J. Chem. Phys. **125**, 234109 (2006).
[61]O. A. Vydrov, J. Heyd, A. V. Krukau, and G. E. Scuseria, J. Chem. Phys. **125**, 074106 (2006).
[62]J.-D. Chai and M. Head-Gordon, J. Chem. Phys. **131**, 174105 (2009).
[63]F. Zapata, E. Luppi, and J. Toulouse, J. Chem. Phys. **150**, 234104 (2019).
[64]R. van Leeuwen and E. J. Baerends, Phys. Rev. A **49**, 2421 (1994).
[65]N. Gauriot, V. Véniard, and E. Luppi, J. Chem. Phys. **151**, 234111 (2019).
[66]M. Monfared, E. Irani, and R. Sadighi-Bonabi, J. Chem. Phys. **148**, 234303 (2018).
[67]X. Chu and G. C. Groenenboom, Phys. Rev. A **93**, 013422 (2016).
[68]T. T. Gorman *et al.*, J. Chem. Phys. **150**, 184308 (2019).
[69]K. Kaufmann, W. Baumeister, and M. Jungen, J. Phys. B: At. Mol. Opt. Phys. **22**, 2223 (1989).
[70]Y. Shao *et al.*, Phys. Chem. Chem. Phys. **8**, 3172 (2006).
[71]E. Luppi and M. Head-Gordon, J. Chem. Phys. **139**, 164121 (2013).
[72]E. Coccia, Mol. Phys. **118**, e1769871 (2020).
[73]S. Klinkusch, P. Saalfrank, and T. Klamroth, J. Chem. Phys. **131**, 114304 (2009).
[74]D. Shiner, J. M. Gilligan, B. M. Cook, and W. Lichten, Phys. Rev. A **47**, 4042 (1993).
[75]A. Hamnett, W. Stoll, and C. E. Brion, J. Electron. Spectrosc. Related Phenom. **8**, 367 (1976).
[76]K. Kimura, S. Katsumata, Y. Achiba, T. Yamazaki, and S. Iwata, *Handbook of HeI Photoelectron Spectra* (Japan Scientific Societies Press, Tokyo und Halstead Press, New York, 1981).
[77]R. Reiff, T. Joyce, A. Jaroń-Becker, and A. Becker, J. Phys. Commun. **4**, 065011 (2020).
[78]Y. Li, T. Sato, and K. L. Ishikawa, Phys. Rev. A **99**, 043401 (2019).
[79]M. Lein, N. Hay, R. Velotta, J. P. Marangos, and P. L. Knight, Phys. Rev. A **66**, 023805 (2002).
[80]J. Heslar, D. A. Telnov, and S.-I. Chu, Phys. Rev. A **83**, 043414 (2011).
[81]H.-L. Sun, W.-T. Peng, and J.-D. Chai, RSC Adv. **6**, 33318 (2016).
[82]M. R. Mack, D. Whitenack, and A. Wasserman, Chem. Phys. Lett. **558**, 15 (2013).
[83]X. Chu and S.-I. Chu, Phys. Rev. A **64**, 063404 (2001).
[84]A. Wardlow and D. Dundas, Phys. Rev. A **93**, 023428 (2016).